ACS APPLIED MATERIALS & INTERFACES

www.acsami.org

Research Article

2D-Self-Assembled Organic Materials in Undoped Hole Transport Bilayers for Efficient Inverted Perovskite Solar Cells

Isaac G. Sonsona, Manuel Carrera, Miriam Más-Montoya,* Rafael S. Sánchez, Patricio Serafini, Eva M. Barea, Iván Mora-Seró,* and David Curiel*

Cite This: *ACS Appl. Mater. Interfaces* 2023, 15, 22310−22319

Read Online

ACCESS | Metrics & More | Article Recommendations | Supporting Information

ABSTRACT: Interfaces between photoactive perovskite layer and selective contacts play a key role in the performance of perovskite solar cells (PSCs). The properties of the interface can be modified by the introduction of molecular interlayers between the halide perovskite and the transporting layers. Herein, two novel structurally related molecules, 1,3,5-tris(α-carbolin-6-yl)benzene (**TACB**) and the hexamethylated derivative of truxenotris(7-azaindole) (**TTAI**), are reported. Both molecules have the ability to self-assemble through reciprocal hydrogen bond interactions, but they have different degrees of conformational freedom. The benefits of combining these tripodal 2D-self-assembled small molecular materials with well-known hole transporting layers (HTLs), such as PEDOT:PSS and PTAA, in PSCs with inverted configuration are described. The use of these molecules, particularly the more rigid **TTAI**, enhanced the charge extraction efficiency and reduced the charge recombination. Consequently, an improved photovoltaic performance was achieved in comparison to the devices fabricated with the standard HTLs.

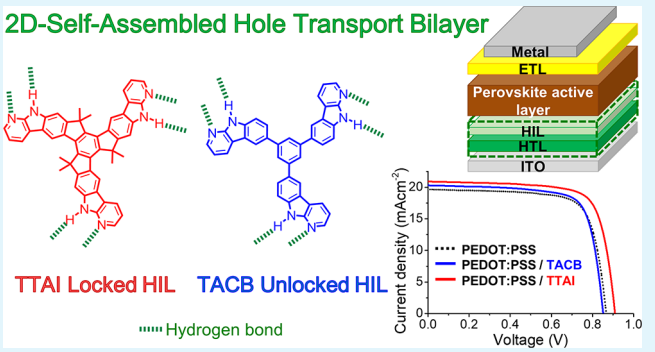

KEYWORDS: *self-assembly, interface engineering, hole transporting material, perovskite solar cell*

INTRODUCTION

The first photovoltaic device based on an organic−inorganic hybrid perovskite material was reported by Miyasaka and colleagues in 2009.[1] The power conversion efficiency (PCE) of that pioneer solar cell was merely of 3.8%. Since then, the efficiency of perovskite solar cells (PSCs) has remarkably improved to reach a certified record of 25.7%.[2] The extraordinary properties of perovskite (wide sunlight absorption range with high extinction coefficients,[3] low exciton binding energy,[4] ambipolar charge transport with high mobilities,[5,6] long charge diffusion length,[7] low trap density,[8] and versatile processability)[9] have made these materials a promising alternative for the future generation of solar cells. More importantly, these properties admit the possibility of being further tuned and optimized through the perovskite composition.[10] Beyond halide perovskite intrinsic properties, the role of interfaces has been crucial for the development of high performance PSCs.[11] In this sense, the device engineering has also allowed the continuous improvement of the performance of PSCs,[12,13] where it has been shown to be the critical effect of the interfaces between photoactive perovskite layer and transport layers. Consequently, it is worth highlighting the contribution of interfacial layers, deposited between the active perovskite film and the transport layers, hereafter denoted as hole interfacial layer (HIL), to the progress of PSCs.[14,15] These layers play critical roles for the optimum performance of the solar cell such as control of the selective charge carrier transport, protection of the active layer, and modulation of the perovskite morphology. To accomplish these functions, interfacial layers must meet certain requirements: transparency to the solar radiation; adequate and balanced charge transport; good energy level alignment with adjacent materials; soft and homogeneous thin-film forming ability compatible with the perovskite layer processing. A myriad of organic (small molecules and polymers) and inorganic materials have demonstrated their suitability to improve the solar cell performance.[16−21] In general, the best results have been reported for devices incorporating doped interfacial layers, particularly in the case of hole transporting materials.[22] However, it is known that dopants commonly affect the degradation of the PSCs,[23−25] and, accordingly, the research focused on dopant-free HTLs has taken much interest.[26−30]

Received: December 23, 2022
Accepted: April 13, 2023
Published: April 26, 2023

Scheme 1. Synthetic Route for TACB and TTAI

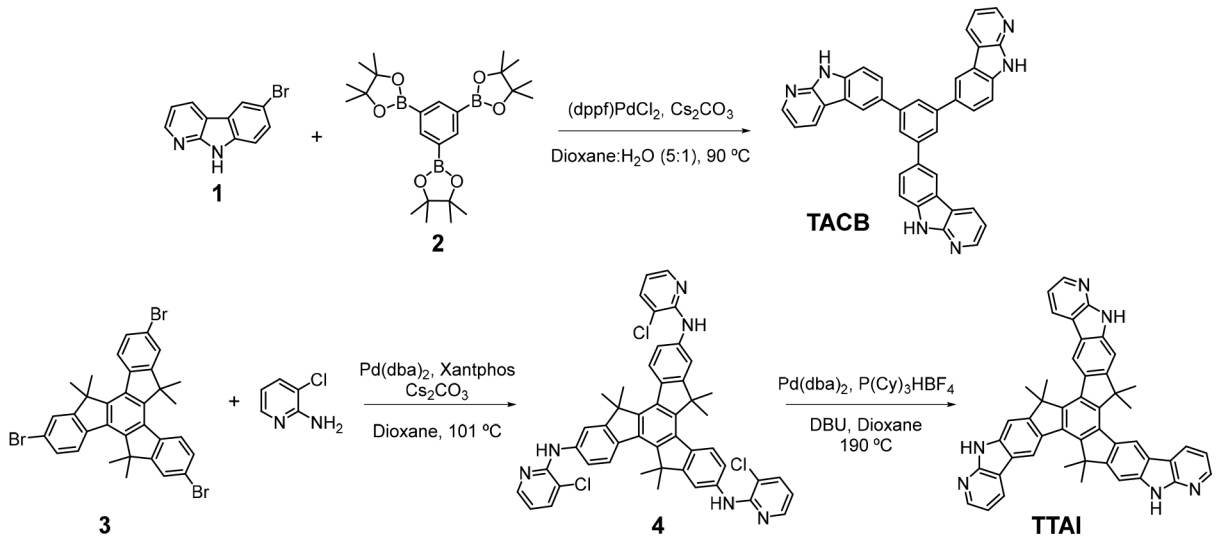

Among the different PSCs configurations, the inverted device architecture (p-i-n) shows, in general, lower efficiencies, with certified PCE record of 23.6%,[31] than the conventional configuration (n-i-p). Nevertheless, the former possesses the great advantage of requiring lower annealing temperatures during the fabrication, which enables the manufacturing of flexible devices that are compatible with roll-to-roll processing for mass production.[32] Interestingly, these convenient processing features widen the assortment of adequate materials and procedures for the sequential deposition of multilayers. Moreover, these methodologies are suitable for the fabrication of tandem devices.[33] Currently, the efficiency of inverted solar cells still lags behind that of the conventional devices, mainly due to lower V_{OC} and nonradiative recombination losses. Since these features are related to interfacial defects, the engineering of interfacial layers can efficiently contribute to the optimization of inverted PSCs. In this regard, we have focused our attention in the two most frequently used hole transporting materials in inverted PSCs, namely poly(3,4-ethylenedioxythiophene):poly(styrenesulfonate) (PEDOT:PSS)[34] and poly[bis(4-phenyl)(2,4,6-trimethylphenyl)amine] (PTAA).[35] Despite the common use of these materials, the hygroscopic and acidic nature of PEDOT:PSS affects the stability of the PSC. Concerning PTAA, it presents issues related to the surface energy and wettability required for the subsequent deposition of the perovskite layer, thus affecting the fabrication and corresponding performance of the PSCs. Accordingly, the deposition of an interfacial layer between the HTL and the perovskite can contribute to minimize these problems and allow a fine-tuning at the interface toward an optimum energy level matching between adjacent materials. This has been demonstrated for PEDOT:PSS and/or PTAA in hole transporting bilayers (HTBLs),[36,37] where the detrimental charge recombination has been notably reduced by inserting inorganic materials such as copper salts (CuSCN or CuI),[38,39] metal oxides (V_2O_5, NiO_X, or MoO_3), or phosphorene.[40] The combination with polyelectrolytes or functionalized reduced graphene oxide has also led to improved performances.[41−43] Nevertheless, with a few exceptions,[44,45] organic small molecules have been barely explored for this purpose.

In this work, we present a comparative study between two tripodal small molecules that can be easily integrated in the inverted PSC configuration. The use of these interfacial layers improves the performance of inverted PSCs using both PEDOT:PSS and PTAA as HTLs. We have previously demonstrated that hydrogen bond-directed self-assembly of conjugated systems represent a useful approach to increase the robustness of organic semiconductors and to preserve the structural integrity of these materials.[46,47] Moreover, we have also proved how self-assembly can be used to control the molecular arrangement in the solid state thanks to the strength of hydrogen bonding between rationally located donor and acceptor sites and how self-assembled HTLs benefit the performance of PSCs.[48,49] This approach has been further adapted to the development of 2D materials that can extend the self-organization of the molecules within planar domains.[50] Based on these results, herein we have investigated the use of 2D-self-assembled π-expanded tripodal molecules as dopant-free HILs. Their condition of small molecules enables deposition by thermal evaporation that improves the control of the thickness and morphology of the thin film. Additionally, their ability to self-assemble remarkably decreases the solubility of these molecules, favoring their compatibility with the solution processing of subsequent top-layers in the solar cell. With the aim of going a step forward in the understanding of the structure−property relationship in self-assembled materials, we have synthesized two analogous molecules, namely 1,3,5-tris(α-carbolin-6-yl)benzene (**TACB**) and the 5,5,10,10,15,15-hexamethylated derivative of truxenotris(7-azaindole) (**TTAI**) (Scheme 1), that integrate three 7-azaindole units for directing the 2D-self-assembly through reciprocal hydrogen bonds but differ in the rotational freedom of the three arms. Since the planarity and the conformational freedom are important structural features when dealing with the charge transport properties of conjugated molecular systems,[51−53] we investigate this effect on hole transporting bilayers. To this end, the rotationally free α-carboline fragments, connected to a central benzene core in **TACB**, are locked in **TTAI** by linking the central benzene and each peripheral substructure with three carbon bridges, leading to a truxene-like core. As will be discussed further, both materials exhibited suitable properties to be incorporated as interfacial layers in PSCs. Moreover, we have observed that the use of these self-assembled 2D materials in HTBLs improves the charge extraction efficiency and

https://doi.org/10.1021/acsami.2c23010
ACS Appl. Mater. Interfaces 2023, 15, 22310−22319

reduces the charge recombination, resulting in a better performance of inverted perovskite solar cells when compared to the devices fabricated with the standard HTLs.

EXPERIMENTAL SECTION

General. Reagents and solvents used for the synthesis, purification, and characterization of the reported compounds were commercially available and used without any purification treatment. Unless stated otherwise, all reactions were performed under nitrogen atmosphere. Final products were purified by gradient sublimation (pressure $<10^{-6}$ mbar) to obtain high purity materials. ^{1}H NMR and ^{13}C NMR spectra were recorded at room temperature on a Bruker AV400 or AV300 spectrometer having frequencies of 400 or 300 MHz for proton nuclei and 101 or 75.5 MHz for carbon nuclei. The residual peak of the deuterated solvent was used as reference for the chemical shifts. Mass spectra were measured on an HPLC-MS TOF 6220 instrument. Melting points were measured in a Reichert instrument and are not corrected. Thermogravimetric analysis (TA) was performed on a SDT 2960 analyzer from TA Instruments under inert atmosphere (heating rate: 10 °C min^{-1}). Differential scanning calorimetry (DSC) was performed on a TA Instrument DSC 2920, and the second heating and cooling cycle was analyzed. Absorption spectra were measured on a Cary 5000 UV−vis-NIR spectrophotometer. Emission spectra were recorded on a Jobin Yvon Fluorolog 3−22 luminescence spectrometer using a 450-W xenon lamp, double grating monochromators, and a TBX-04 photomultiplier. Cyclic voltammetry experiments were performed in dichloromethane using a BAS potentiostat. A platinum coated electrode was employed as working electrode, a Pt wire as counter electrode, Ag/AgCl as reference electrode, and the ferrocene/ferrocenium (Fc/Fc^{+}) couple as internal reference. The scan rate was 100 mV s^{-1}. Tetrabutylammonium hexafluorophosphate (0.1 M) was the supporting electrolyte.

Synthetic Methods. *1,3,5-Tris(α-carbolin-6-yl)benzene, **TACB**.* 6-Bromo-α-carboline (494 mg, 2 mmol), 1,3,5-tris(4,4,5,5-tetramethyl-1,3,2-dioxaborolan-2-yl)benzene (273 mg, 0.6 mmol), dichloro-[1,1′-bis(diphenylphosphino)ferrocene]palladium(II) (76.6 mg, 0.1 mmol), and cesium carbonate (795 mg, 2.4 mmol) were introduced in a Schlenk flask, and nitrogen atmosphere was made to the system through vacuum/nitrogen cycles. In another flask, a mixture of water (10 mL) and 1,4-dioxane (50 mL) was bubbled with nitrogen for 15−20 min. Then this mixture was added to the Schlenk flask and nitrogen bubbling was continued for 10 additional minutes. Finally, the reaction mixture was introduced in preheated oil bath at 90 °C and it was allowed to react at that temperature with magnetic stirring. After 60 h, the Schlenk flask was cooled down to room temperature and water was added to the reaction mixture, obtaining a suspension that was stirred for 10 min. Then the solid was collected by filtration, washed with water, and dried. The brown solid obtained was purified by silica gel column chromatography using THF as eluent, followed by trituration with MeOH and CH_2Cl_2, yielding the desired product as a light yellow solid (127 mg, 37% yield). Mp > 300 °C. ^{1}H NMR (400 MHz, DMSO-d_6), δ: 11.90 (s, 3H), 8.79 (d, J = 1.5 Hz, 3H), 8.67 (dd, J = 7.7, 1.5 Hz, 3H), 8.45 (dd, J = 4.8, 1.6 Hz, 3H), 8.11 (s, 3H), 8.07 (dd, J = 8.5, 1,8 MHz, 3H), 7.66 (d, J = 8.4 Hz, 3H), 7.26 (dd, J = 7.7, 4.8 Hz, 3H) ppm. ^{13}C NMR (APT) (75.5 MHz, DMSO-d_6), δ: 152.4 (C), 146.3 (CH), 142.4 (C), 138.5 (C), 132.2 (C), 128.9 (CH), 126.1 (CH), 123.7 (CH), 121.2 (C), 119.9 (CH), 115.6 (C), 115.2 (CH), 111.7 (CH) ppm. HRMS (ESI), m/z, $[M + H]^+$ Calcd for $C_{39}H_{25}N_6$: 577.2135, Found: 577.2148.

*5,5,10,10,15,15-Hexamethyl-N^2,N^7,N^{12}-tris(3-chloropyridin-2-yl)-truxene-2,7,12-triamine, **4**.* In a two-neck round-bottom flask under nitrogen atmosphere, stirring, and at room temperature, dry dioxane (20 mL) was added via syringe to a mixture of compound **3** (330 mg, 0.50 mmol), 2-amino-3-chloropyridine (384 mg, 2.99 mmol), bis(dibenzylideneacetone)palladium (0) (14.3 mg, 0.025 mmol), 4,5-bis(diphenylphosphino)9,9-dimethylxanthene (Xantphos) (21.6 mg, 0.037 mmol), and cesium carbonate (0.97 g, 2.99 mmol). The reaction was heated at reflux temperature and the progress of the reaction monitored by thin layer chromatography. After 24 h, $Pd(dba)_2$ (14.3 mg, 0.025 mmol) and Xantphos (21.6 mg, 0.037 mmol) were added again and the reaction was allowed to continue for 24 more hours. After this time, the reaction flask was cooled down and the solvent removed under vacuum. The resulting crude was purified by silica gel column chromatography (Hexane/THF, 7/3) to obtain the product as a yellow solid (267 mg, 67% yield). Mp: 298 °C. ^{1}H NMR (400 MHz, $CDCl_3$), δ: 8.26 (d, J = 8.6 Hz, 3H), 8.22 (dd, J = 4.8, 1.6 Hz, 3H), 7.83 (dd, J = 8.6, 2.2 Hz, 3H), 7.69 (d, J = 2.1 Hz, 3H), 7.62 (dd, J = 7.7, 1.6 Hz, 3H), 7.21 (s, 3H), 6.76 (dd, J = 7.7, 4.9 Hz, 3H), 1.91 (s, 18H) ppm. ^{13}C NMR (APT) (75.5 MHz, $CDCl_3$), δ: 158.9 (C), 151.4 (C), 146.6 (C), 146.1 (CH), 138.6 (C), 136.8 (CH), 135.6 (CH), 131.8 (C), 126.2 (CH), 118.0 (CH), 116.3 (C), 115.3 (CH), 114.0 (CH), 47.0 (C), 24.3 (CH_3) ppm. HRMS (ESI) m/z: $[M + H]^+$ Calcd for $C_{48}H_{40}Cl_3N_6$: 807.2357; Found: 807.2358.

*5,5,10,10,15,15-Hexamethyltruxeno[2,3-b:7,8-b′:12,13-b′′]tri(7-azaindole), **TTAI**.* The reaction was performed in a sealed tube previously loaded with dry dioxane (8.5 mL), compound **4** (230 mg, 0.29 mmol), bis(dibenzylideneacetone)palladium (0) (98.3 mg, 0.17 mmol), tricyclohexylphosphonium tetrafluoroborate (127 mg, 0.342 mmol), and 1,8-diazabicylo(5.4.0)undec-7-ene (0.40 mL, 2.72 mmol). After the reaction mixture was bubbled with nitrogen for 10 min, the tube was sealed and the reaction was stirred for 5 days at 190 °C. Once the reaction cooled down, water (50 mL) was added to obtain a yellow suspension that was filtered under vacuum and sequentially washed with water (3 × 50 mL), diethyl ether (3 × 10 mL), and chloroform (3 × 20 mL). The pure product was isolated as a pale gray solid (156 mg, 79% yield). Mp: > 300 °C. ^{1}H NMR (400 MHz, $CDCl_3$ (1% TFA-d)), δ: 13.22 (brs, 3H), 9.07 (s, 3H), 9.04 (dd, J = 7.5, 0.7 Hz, 3H), 8.47 (dd, J = 5.9, 0.8 Hz, 3H), 8.07 (s, 3H), 7.63 (dd, J = 7.6, 6.1 Hz, 3H), 2.12 (s, 18H) ppm. ^{13}C NMR (APT) (75.5 MHz, $CDCl_3$ (1% TFA-d)), δ: 161.3 (C), 148.1 (C), 145.6 (C), 139.4 (C), 135.6 (C), 134.9 (CH), 133.3 (CH), 132.3 (C), 123.7 (C), 118.5 (C), 118.2 (CH), 114.8 (CH), 108.1 (CH), 47.3 (C), 24.6 (CH_3) ppm. HRMS (ESI) m/z: $[M-H]^-$ Calcd for $C_{48}H_{35}N_6$: 695.2929; Found: 695.2923.

X-ray Diffraction. Single crystals of **TACB** suitable for X-ray diffraction measurements were grown by slow evaporation of a DMSO solution. Intensities were registered at low temperature on a Bruker D8QUEST diffractometer using monochromated Cu Kα radiation (λ = 1.54178 Å). Absorption corrections were based on multiscans (program SADABS). Structures were refined anisotropically using SHELXL-2018. Hydrogen atoms were included using a riding model. The NH hydrogen was located in a difference synthesis and was refined as free. CCDC 2225042 contains the supplementary crystallographic data for **TACB**. These data can be obtained free of charge from The Cambridge Crystallographic Data Centre via www.ccdc.cam.ac.uk/structures.

RESULTS AND DISCUSSION

Synthesis and Characterization. The synthetic routes designed for the novel small molecules are outlined in Scheme 1. The more conformationally free **TACB** was obtained via a 3-fold Suzuki-Miyaura[54] cross-coupling reaction between 6-bromo-α-carboline (**1**)[55,56] and the corresponding 1,3,5-tris(4,4,5,5-tetramethyl-1,3,2-dioxaborolan-2-yl)benzene, **2**. As far as the conformationally locked **TTAI** synthesis is concerned, first, the 5,5,10,10,15,15-hexamethyl-2,7,12-tribromotruxene, **3**,[57,58] was subject to a triple Pd-catalyzed Buchwald-Hartwig[59] C−N coupling with 2-amino-3-chloropyridine. Subsequently, a Pd-mediated intramolecular cyclization of the resulting product, **4**, afforded the rigid skeleton of **TTAI**. The structure of all the intermediate and final products was confirmed by proton and carbon nuclear magnetic resonance spectroscopies and high-resolution mass spectrometry. Further details can be found in the Supporting Information. Additionally, final products were subject to gradient sublimation to obtain highly pure materials.

https://doi.org/10.1021/acsami.2c23010
ACS Appl. Mater. Interfaces 2023, 15, 22310−22319

Density functional theory (DFT) calculations confirmed the conformational differences between **TACB** and **TTAI**. The three peripheral α-carbolines in **TACB** are not coplanar but are rotated (36.8−39.5°) with respect to the plane defined by the central benzene core to minimize the steric hindrance (Figure S9a). Conversely, the fused polyheteroaromatic structure of **TTAI** presents a completely planar geometry (Figure S9b). Besides, three 7-azaindole units have been rationally located in the periphery of the conjugated systems, **TACB** and **TTAI**, to direct the 2D-supramolecular self-assembly through reciprocal hydrogen bonding between the hydrogen bond donor sites ($N-H_{pyrrole}$) and the hydrogen bond acceptor sites ($N_{pyridine}$) (Figure 1a). This building bock has been previously demonstrated to be an excellent synthon for controlling the molecular arrangement in the solid state.[47,49,60] Hydrogen bond-directed self-assembly has also been confirmed by the single-crystal X-ray diffraction of **TACB** (Figure S10). The supramolecular self-assembly bestows a significant thermal robustness to the novel materials that display high decomposition temperatures of 508 °C (**TACB**) and 512 °C (**TTAI**) (Figure S7).

The optical properties of the materials were analyzed by absorption spectroscopy (Figure 1b and Table 1). **TACB** showed a broad band at 296 nm, ascribed to $\pi-\pi^*$ transitions. Concerning **TTAI**, the most prominent band is bathochromically shifted to 317 nm due to the more extended conjugation in this conformationally locked molecule. Besides, a small shift toward lower energy was detected in the thin film spectra with respect to those measured in solution owing to the stronger intermolecular interactions established in the solid state. In any case, it is worth noticing that no absorption was observed above 400 nm, making these molecules transparent to the visible radiation. This feature implies that the novel molecules are good candidates to be incorporated as interfacial materials since they will not interfere with the sunlight absorption at the perovskite layer. Consequently, wide optical gaps were estimated from the onset of the lowest energy band of the thin film absorption spectra with values of 3.59 and 3.16 eV for **TACB** and **TTAI**, respectively.

Cyclic voltammetry showed irreversible voltammograms for both compounds, with **TACB** presenting a higher anodic peak potential (1078 mV) than the rigid **TTAI** (1064 mV) (Figure S11). Consequently, a slightly deeper HOMO energy was estimated from the oxidation onset of **TACB** (−5.33 eV) than **TTAI** (−5.25 eV) (Figure 1b). The LUMO energies (**TACB**: − 1.74 eV; **TTAI**: − 2.09 eV) were calculated by adding the optical gaps to the HOMO energy. Additionally, DFT theoretical studies allowed the determination of the isosurfaces of the frontier molecular orbitals (Figure 1c). The spatial representation of the HOMO on the **TACB** structure revealed a larger contribution of the central benzene and of one of the α-carboline units. The LUMO isosurface also displayed larger coefficients localized in one of the arms of the tripodal structure with the other two showing a smaller contribution and without a clear participation of the benzene core. As far as **TTAI** is concerned, the HOMO is mainly distributed over two arms of the molecule and this also occurs for the LUMO isosurface.

The estimated energy levels present a correct alignment with the HOMO energies of PEDOT:PSS (−5.1 eV) and PTAA (−5.2 eV), as well as with the valence band (−5.9 eV) of the triple-cation perovskite, that will be used as active layer (Figure S12). The different combinations of HTBLs formed with each molecular material, **TACB** and **TTAI**, define an energy gradient that could improve the driving force for the hole

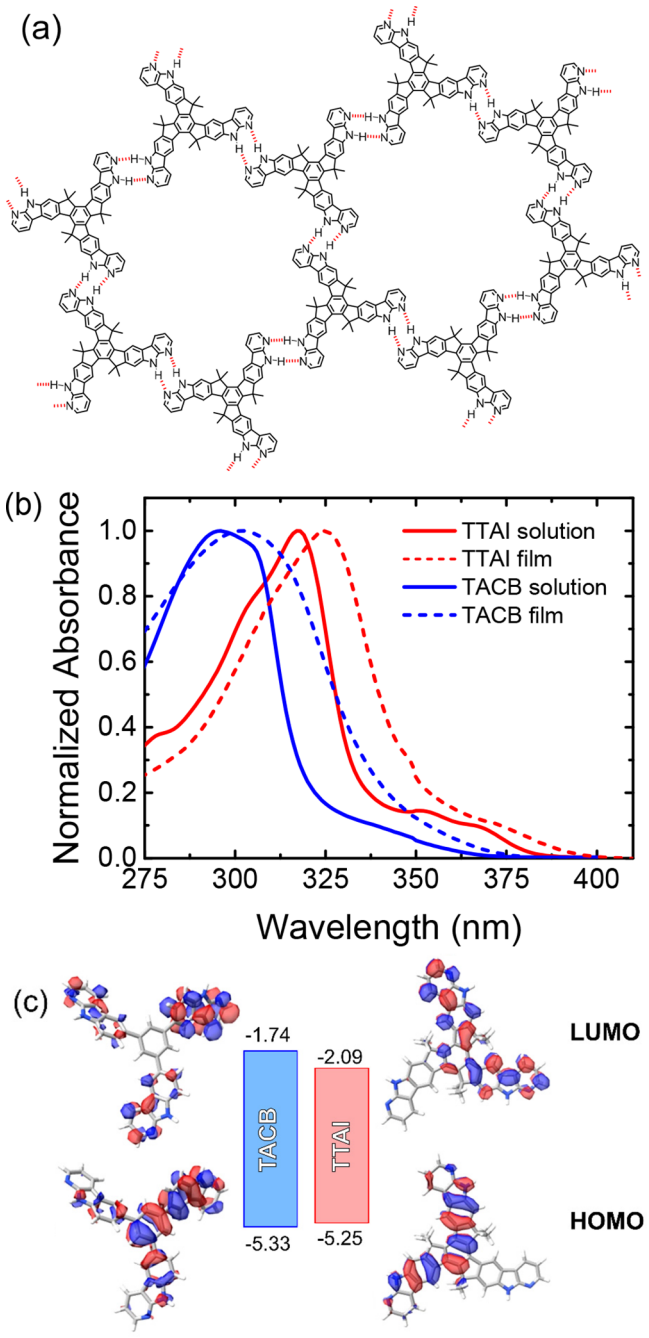

Figure 1. (a) Idealized view of 2D-self-assembled **TTAI**. (b) Normalized absorption spectra in DMF solution and as thin film. (c) Energy diagram and computed frontier molecular orbitals (0.02 isovalue). Experimental HOMO and LUMO energy values are given in eV.

Table 1. Optical and Electrochemical Properties

material	$\lambda_{max.}^{abs.\ sol.}$ [nm]	$\lambda_{max.}^{abs.\ film}$ [nm]	E_g^{film} [eV][a]	E_{HOMO} [eV][b]	E_{LUMO} [eV][c]
TACB	296	302	3.59	−5.33	−1.74
TTAI	317	325	3.16	−5.25	−2.09

[a] E_g^{film} [eV] = 1240/ λ_{onset}^{film} [nm]. [b] $E_{HOMO} = -4.8 - (E_{onset} - E_{Fc,\ onset})$. [c] $E_{LUMO} = E_{HOMO} + E_g$.

https://doi.org/10.1021/acsami.2c23010
ACS Appl. Mater. Interfaces 2023, 15, 22310−22319

extraction (Figure S12). Additionally, the high LUMO energies confirm the suitability of these materials to block wrongly directed electrons.

Charge transport measurements have been performed on single carrier devices fabricated with the architecture ITO/MoO_3/HTM/MoO_3/Ag. The $J-V$ characteristics corresponding to the space-charge-limited current regime have been fitted to the Murgatroyd model (Figure S13).[61] As it could be inferred from DFT models, showing a planar skeleton for **TTAI** and a twisted structure for **TACB**, the hole mobility determined for **TTAI** (4.8×10^{-5} cm^2 V^{-1} s^{-1}) is almost 2 orders of magnitude higher than for **TACB** (7.1×10^{-7} cm^2 V^{-1} s^{-1}), presumably due to the better $\pi-\pi$ intermolecular interactions within the bulk hydrogen bonded material.

Solar Cells Fabrication and Characterization. To explore the ability of the novel compounds to work as HIMs, they were incorporated to devices with inverted architecture according to the sequence: indium tin oxide (ITO)/HTL/HIM/perovskite/fullerene (C_{60})/bathocuproine (BCP)/Ag. Different thicknesses of the interfacial materials were tested during the device fabrication, showing that 15 nm of **TACB** and 10 nm of **TTAI** offered better results (Tables S3 and S4). Either PEDOT:PSS or PTAA has been selected as HTL due to its extensive use in PSCs. The active layer is constituted by a triple-cation mixed-halide perovskite with the composition $Cs_{0.05}(MA_{0.15}FA_{0.85})_{0.95}Pb(Br_{0.15}I_{0.85})_3$, where MA stands for methylammonium and FA for formamidinium. Moreover, devices without HIMs were also fabricated as reference samples. Further details about the device fabrication can be found in the Supporting Information.

Field emission scanning electron microscopy (FESEM) was employed to investigate the effect of the subjacent material on the morphology of the perovskite layers deposited atop (Figure 2). The FESEM images of the perovskite surface with and without HIMs show compact and uniform films. Nevertheless, the average grain size decreased for the PEDOT:PSS bilayers with **TACB** and **TTAI** (181 and 186 nm, respectively) compared to the simple PEDOT:PSS (242 nm). The average perovskite grain size less significantly decreased from 245 nm for PTAA to 201 and 225 nm for PTAA/**TACB** and PTAA/**TTAI** bilayers, respectively.

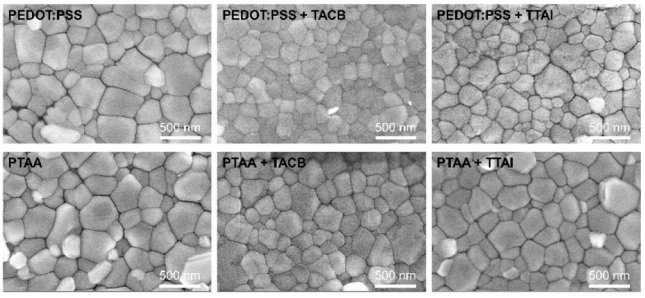

Figure 2. Top-view FESEM images of the photoactive perovskite layers grown on the different HTLs with and without **TACB** and **TTAI** HIMs.

The current density–voltage curves of the best devices are shown in Figure 3 and Figure S14, while the photovoltaic parameters for those solar cells and the average values for each device are summarized in Table 2. The integration of the HIM combining the PEDOT:PSS/**TACB** HTBL does not noticeably change the average PCE compared to bare PEDOT:PSS.

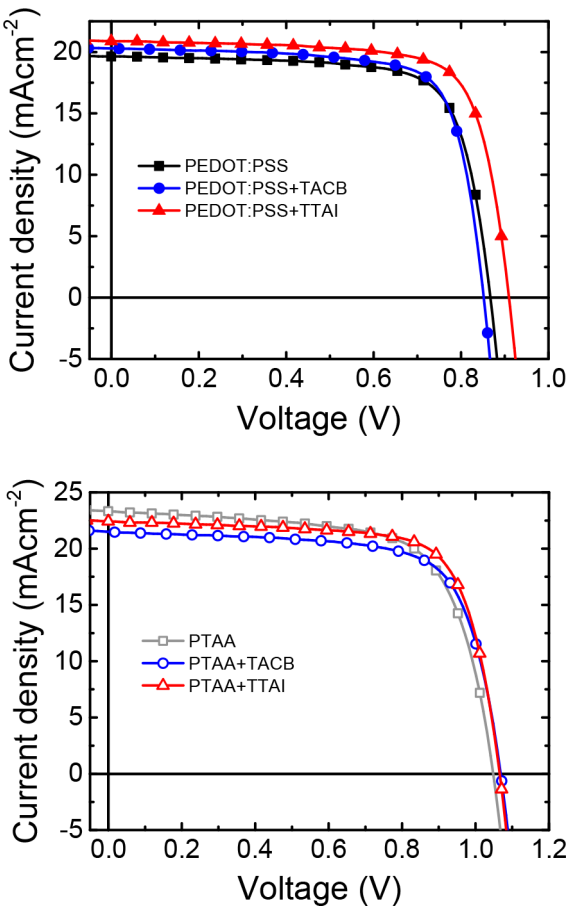

Figure 3. Current density–voltage characteristics under AM1.5 G illumination of the best performing devices.

However, the use of the conformationally locked **TTAI** causes a manifest improvement of all the device parameters, see Table 2.

PTAA-based solar cells present higher performance than PEDOT:PSS, in agreement with previous literature.[62] On average, samples with a simple PTAA HTL present higher PCE, short circuit current density (J_{SC}), and open circuit voltage (V_{OC}) but a lower fill factor (FF) than PEDOT:PSS reference devices. Interestingly, the PTAA/HIM bilayer induces, in general, a FF and V_{OC} enhancement but a J_{SC} decrease. The lower J_{SC} more clearly affects the performance of the PTAA/**TACB** combination. Conversely, the effect on J_{SC} is not significant for the conformationally rigid **TTAI**. As a result, the PTAA/**TTAI** combination performs better than bare PTAA. Note that the different interfacial properties of PEDOT:PSS and PTAA are evidenced by the standard hysteresis observed for the former while inverted hysteresis for the latter, with higher apparent device performances for the forward scan. This behavior has been attributed to a different interface polarization.[63] In this regard, it is worth highlighting that, when fabricating the devices with HTBLs, the hysteresis index (HI)[64] is perceptively reduced whether **TACB** or **TTAI** is used, particularly in combination with PTAA. Thus, a beneficial interfacial modification has been proved by the incorporation of the HIMs.

The photocurrent densities determined from the integration of the external quantum efficiency (EQE) spectra (Figure S14b) are in good agreement, within the accepted deviation,[65]

https://doi.org/10.1021/acsami.2c23010
ACS Appl. Mater. Interfaces 2023, 15, 22310–22319

Table 2. Device Metrics[a] Extracted from the $J-V$ Characteristics Measured in Different Scan Directions at Simulated AM1.5G Illumination, 100 mW cm^{-2}

HTL	scan direction	J_{SC} [mA/cm^2]	V_{OC} [V]	FF [%]	PCE [%]	HI[b]
PEDOT:PSS	Reverse	19.64 (19.90 ± 0.38)	0.87 (0.81 ± 0.06)	74.23 (72.87 ± 0.91)	12.64 (11.72 ± 0.90)	0.031
	Forward	19.31 (19.68 ± 0.44)	0.83 (0.78 ± 0.04)	73.38 (73.01 ± 0.70)	11.80 (11.27 ± 0.54)	
PEDOT:PSS/**TACB**	Reverse	20.29 (19.03 ± 0.58)	0.85 (0.80 ± 0.05)	74.86 (75.51 ± 1.47)	12.94 (11.56 ± 1.01)	0.033
	Forward	19.95 (18.86 ± 0.53)	0.84 (0.80 ± 0.04)	74.47 (74.72 ± 0.92)	12.55 (11.26 ± 0.90)	
PEDOT:PSS/**TTAI**	Reverse	20.89 (21.29 ± 0.32)	0.91 (0.87 ± 0.05)	74.83 (73.47 ± 0.84)	14.22 (13.66 ± 0.78)	0.022
	Forward	20.67 (21.05 ± 0.30)	0.89 (0.85 ± 0.04)	74.20 (73.69 ± 0.66)	13.69 (13.20 ± 0.61)	
PTAA	Reverse	22.55 (21.40 ± 0.67)	1.04 (1.02 ± 0.01)	65.33 (65.46 ± 2.18)	15.31 (14.34 ± 0.78)	0.026
	Forward	23.32 (22.97 ± 0.94)	1.05 (1.04 ± 0.01)	68.18 (67.02 ± 1.40)	16.67 (15.96 ± 0.69)	
PTAA/**TACB**	Reverse	20.66 (19.87 ± 0.54)	1.07 (1.04 ± 0.02)	71.35 (68.95 ± 3.97)	15.85 (14.23 ± 1.13)	0.019
	Forward	21.52 (21.06 ± 0.82)	1.07 (1.05 ± 0.01)	71.18 (69.55 ± 3.60)	16.36 (15.31 ± 0.72)	
PTAA/**TTAI**	Reverse	22.21 (21.24 ± 1.36)	1.07 (1.04 ± 0.03)	70.28 (66.68 ± 4.84)	16.66 (14.87 ± 2.16)	0.006
	Forward	22.44 (22.05 ± 0.68)	1.07 (1.05 ± 0.03)	72.95 (68.33 ± 6.42)	17.44 (15.82 ± 2.15)	

[a]Average values and standard deviation are given in parentheses. [b]Hysteresis index.[62]

with those obtained in the $J-V$ curves. These spectra clearly show the increase in the J_{SC} for the PEDOT:PSS-based bilayers and its decrease for the PTAA-based bilayers that were previously observed; these J_{SC} variations presumably arise from the different EQEs measured within the range between 400 and 600 nm (Figure S14).

With the aim of gaining a deeper understanding about the charge extraction at the perovskite interface, steady-state photoluminescence (PL) spectra of the perovskite films deposited onto simple HTLs or HTL/HIMs bilayers were measured. As can be observed in Figure 4, the shape and position of the PL peak, located at ∼755 nm, remained unchanged independently on the underlying material, thus proving that the slight morphological differences previously observed in the FESEM images do not affect the energy of the emissive transition in the perovskite. Nevertheless, a significant decrease of the active layer PL intensity was induced when a hole transporting material was placed underneath. In particular, the incorporation of the small molecular HIMs induced a larger PL quenching than the control films including PEDOT:PSS or PTAA only. This behavior could be correlated to an improved charge carrier transfer from the photoactive perovskite to the underlying interfacial layer, which is favored by the presence of **TACB** or **TTAI**. It is worth noticing that the interpretation of this phenomenon in terms of an increased surface recombination could be discarded given the higher V_{OC} values of the small molecular based devices in comparison to the control ones.

To investigate the dominant recombination mechanism taking place in the solar cells with the different hole transporting layers, the evolution of the open circuit voltage with the increase of the incident light intensity (I) was also analyzed (Figure 5). The representation of the V_{OC} values as a function of the light intensity is shown in Figure 5. Light ideality factors (n_i) were estimated from the slope of these plots by fitting to the equation:[66]

$$V_{OC} = \frac{E_g}{q} - \frac{n_i k_B T}{q} \ln I \quad (1)$$

where k_B denotes the Boltzmann constant, T the absolute temperature, and q the elementary charge. The calculated light ideality factors are listed in the legend of Figure 5. In general, an ideality factor of 1 is correlated to a predominant band-to-band radiative recombination. Conversely, a value of 2 is associated to a larger contribution of trap-assisted Shockley-Read-Hall (SRH) recombination.[66] In both series of devices, lower ideality factor values were obtained after the incorporation of HIMs. Values closer to unity are assessed for **TTAI**, which demonstrate that the incorporation of this rigid, tripodal, self-assembled material contributes to the reduction of the undesired trap-mediated recombination pathways in the device.

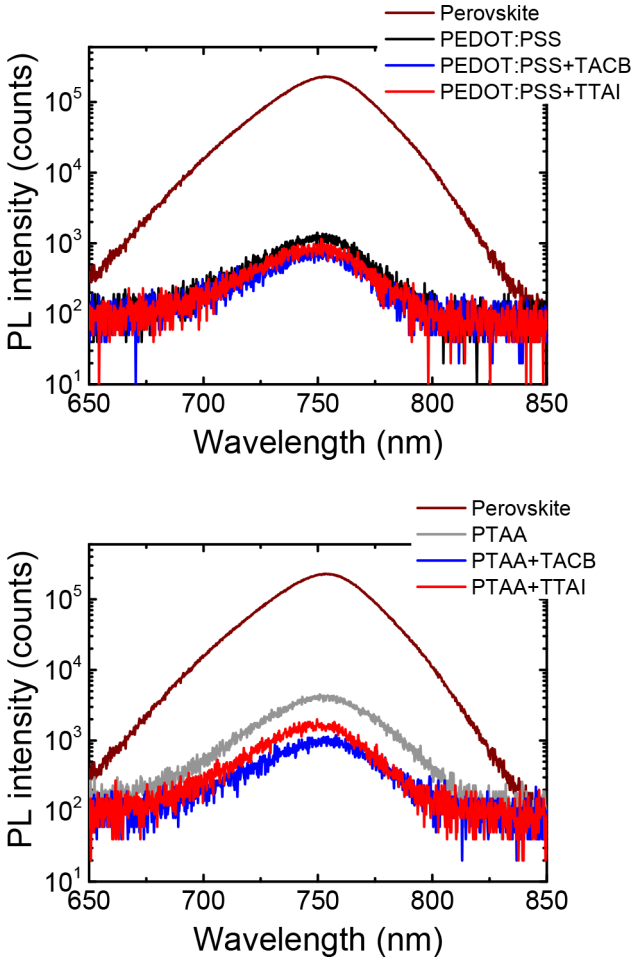

Figure 4. Steady-state PL spectra in semilogarithmic scale of the perovskite film on glass and on the evaluated hole transporting layers.

https://doi.org/10.1021/acsami.2c23010
ACS Appl. Mater. Interfaces 2023, 15, 22310−22319

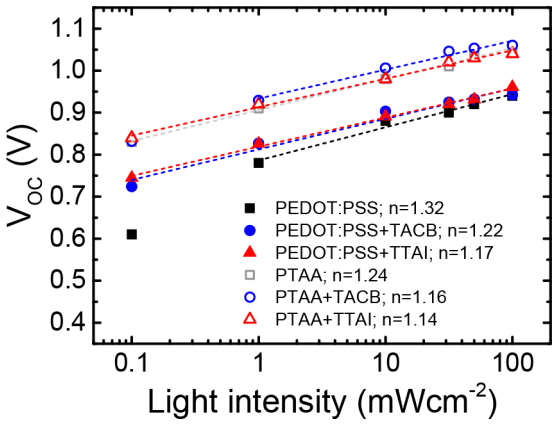

Figure 5. Light intensity dependence of the open-circuit voltage in semilogarithmic scale. Dashed lines represent the linear fits. Ideality factors are shown in the legend.

The charge extraction and recombination processes occurring at the interface between the perovskite and the charge transport layers have been further investigated by studying the dependence of the PL emitted by the complete solar cells with the applied voltage.[67−70] When devices are biased at short-circuit conditions ($V_{app.}$ = 0 V), charge extraction is promoted. Then a better charge extraction would result in a lower PL emission. Upon increasing the applied voltage ($V_{app.}$ = V_{OC}), charge extraction is limited and PL is expected to enhance. Moreover, the radiative enhancement will be more significant when nonradiative recombination is reduced. This trend is observed for the different hole transporting layers and bilayers (Figure 6), except simple PEDOT:PSS, presumably due to its known restricted ability to block electrons[71,72] and, therefore, to minimize the nonradiative charge recombination. The PL enhancement ratio is improved in the devices incorporating HTL/HIM bilayers, being better in the case of **TTAI**. Accordingly, these results seem to indicate that a reduced nonradiative recombination can be achieved by inserting effective HIMs.

Focusing on the devices incorporating **TTAI**, their better performance was further demonstrated by measuring the electroluminescence (EL) of the PSCs (Figure S15). Larger EL intensity was observed when HTL/**TTAI** bilayer was present in comparison to the PEDOT:PSS and PTAA single HTLs. These results clearly reinforce that the HIMs promote a reduction of the nonradiative recombination pathways within the device, which is in good agreement with the previously discussed PL experiments.

Finally, to complete the electrical characterization and understand the effect of 2D-self-assembled π-expanded tripodal molecules (**TACB** and **TTAI**) as interfacial materials, electrochemical impedance spectroscopy (EIS) measurements were performed under 1 sun illumination (voltage range 0 to V_{OC}). The EIS experimental details and the equivalent circuit employed to analyze the data are detailed in the Supporting Information. The acquired impedance data were fitted to an equivalent circuit model including a recombination resistance (R_{rec}) considering the transport resistance negligible, and a series resistance (R_s).[73] Focusing on the best performing devices fabricated with PTAA, the corresponding Nyquist plots exhibited two distinctive arcs located in the low- and high-frequency regions (Figure 7). In agreement with the Z′ values, it is observed that the recombination resistance increases when introducing both **TACB** and **TTAI**, with respect to the reference device made with PTAA only. Accordingly, the device fabricated with **TTAI** presents a lower carrier recombination and, consequently, a higher V_{OC} and *FF* as shown in Table 2.

This enhancement emphasizes the relevance of the structure−property relationship showing how, having **TACB** and **TTAI** similar optoelectronic properties, the conformationally locked **TTAI** presents suitable structural features for better performance in the studied hole transport bilayers.

CONCLUSIONS

In conclusion, two unprecedented small molecular materials with analogous structure but different conformational freedom have been synthesized. The tripodal skeleton of these

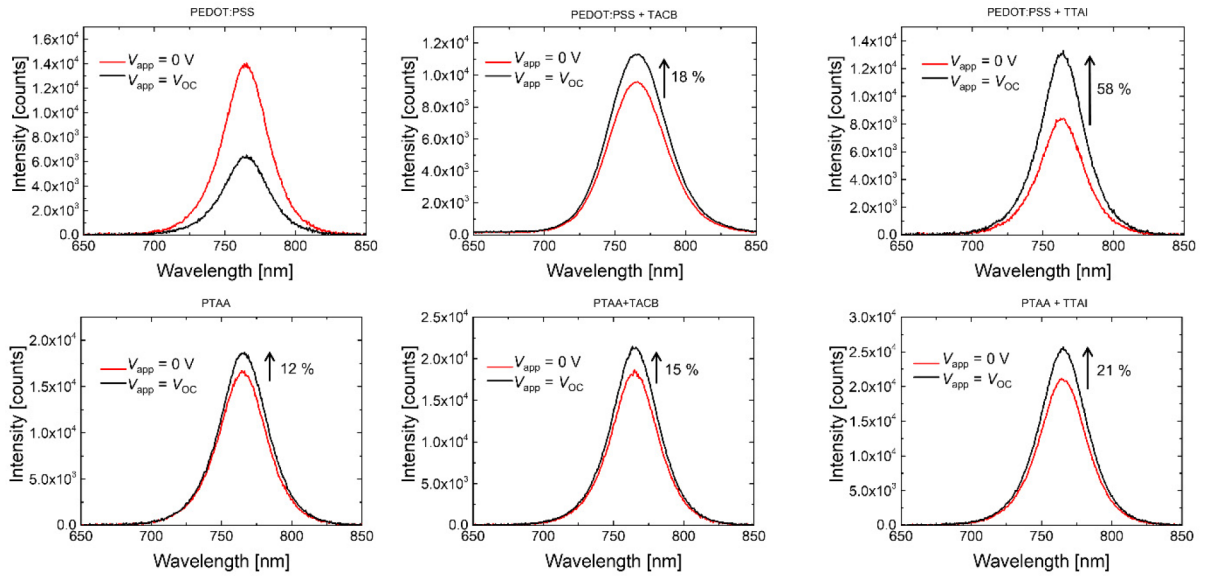

Figure 6. Comparison of the perovskite PL intensity at the active areas of the devices biased at short-circuit (V = 0 V) and at V_{OC}. The PL enhancement ratio is indicated.

https://doi.org/10.1021/acsami.2c23010
ACS Appl. Mater. Interfaces 2023, 15, 22310−22319

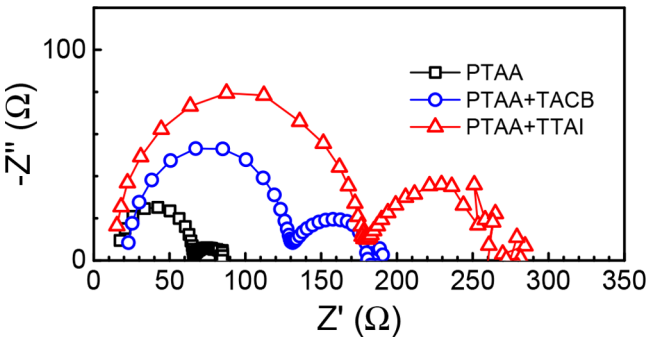

Figure 7. Nyquist plot at V_{OC} for a PTAA single HTL, PTAA/**TACB**, and PTAA/**TTAI** hole transport bilayer.

molecules has been rationally designed to incorporate hydrogen bond donor and hydrogen bond acceptor sites that induce the 2D-self-assembly of these materials. Self-assembly has proved to be a useful tool to improve the robustness of organic thin films. Both molecules, **TACB** and **TTAI**, display a suitable electronic structure to be integrated as hole transporting interfacial materials in perovskite solar cells. This has been demonstrated by the improvement in the performance of the solar cells when combining the novel materials with standard HTLs such as PEDOT:PSS and PTAA, reaching a 17.4% efficiency. The engineering of the hole transporting bilayers, with an adequate energy gradient and intermolecular interactions at the perovskite interface, has led to the reduction of the recombination pathways and the improvement of hole extraction at the perovskite interface. Overall, we can conclude that the strategy based on the self-assembly of interfacial materials such as **TTAI** is a valid approach for the future development of carrier selective transport layers.

■ ASSOCIATED CONTENT

Supporting Information

The Supporting Information is available free of charge at https://pubs.acs.org/doi/10.1021/acsami.2c23010.

NMR spectra; TGA and DSC; computational details; X-ray diffraction of **TACB**; cyclic voltammetry, energy levels diagram, current density vs voltage curves and external quantum efficiency spectra; devices electroluminescence (PDF)

CIF file of TACB crystal structure (CIF)

■ AUTHOR INFORMATION

Corresponding Authors

Miriam Más-Montoya − *Department of Organic Chemistry, Faculty of Chemistry, University of Murcia, 30100 Murcia, Spain;* orcid.org/0000-0001-7161-6804; Email: miriammas@um.es; orcid.org/0000-0001-7161-6804

Iván Mora-Seró − *Institute of Advanced Materials, University Jaume I, 12071 Castelló de la Plana, Spain;* orcid.org/0000-0003-2508-0994; Email: sero@uji.es; orcid.org/0000-0003-2508-0994

David Curiel − *Department of Organic Chemistry, Faculty of Chemistry, University of Murcia, 30100 Murcia, Spain;* orcid.org/0000-0002-6717-6305; Email: davidcc@um.es; orcid.org/0000-0002-6717-6305

Authors

Isaac G. Sonsona − *Department of Organic Chemistry, Faculty of Chemistry, University of Murcia, 30100 Murcia, Spain*

Manuel Carrera − *Department of Organic Chemistry, Faculty of Chemistry, University of Murcia, 30100 Murcia, Spain*

Rafael S. Sánchez − *Institute of Advanced Materials, University Jaume I, 12071 Castelló de la Plana, Spain*

Patricio Serafini − *Institute of Advanced Materials, University Jaume I, 12071 Castelló de la Plana, Spain*

Eva M. Barea − *Institute of Advanced Materials, University Jaume I, 12071 Castelló de la Plana, Spain*

Complete contact information is available at: https://pubs.acs.org/10.1021/acsami.2c23010

Notes

The authors declare no competing financial interest.

■ ACKNOWLEDGMENTS

The authors are grateful for the financial support from the Ministry of Science, Innovation and Universities (Projects RTI2018-101092−B-I00, PID2021-122734OB-I00), Fundación Séneca−Agencia de Ciencia y Tecnología de la Región de Murcia (Projects 20959/PI/18, 22058/PI/22), Programa Estatal de Fomento de la Investigación Científica y Técnica de Excelencia (RED2018-102815-T), and University Jaume I (Project EPCESBI UJI-B2022-08).

■ REFERENCES

(1) Kojima, A.; Teshima, K.; Shirai, Y.; Miyasaka, T. Organometal Halide Perovskites as Visible-Light Sensitizers for Photovoltaic Cells. *J. Am. Chem. Soc.* **2009**, *131*, 6050−6051.

(2) National Renewable Energy Laboratory. *Best Research-Cell Efficiency Chart*; NREL, 2022. https://www.nrel.gov/pv/cell-efficiency.html (accessed 12-2022).

(3) Yin, W.-J.; Shi, T.; Yan, Y. Unique Properties of Halide Perovskites as Possible Origins of the Superior Solar Cell Performance. *Adv. Mater.* **2014**, *26*, 4653−4658.

(4) Savenije, T. J.; Ponseca, C. S.; Kunneman, L.; Abdellah, M.; Zheng, K.; Tian, Y.; Zhu, Q.; Canton, S. E.; Scheblykin, I. G.; Pullerits, T.; et al. Thermally Activated Exciton Dissociation and Recombination Control the Carrier Dynamics in Organometal Halide Perovskite. *J. Phys. Chem. Lett.* **2014**, *5*, 2189−2194.

(5) Zhao, T.; Shi, W.; Xi, J.; Wang, D.; Shuai, Z. Intrinsic and Extrinsic Charge Transport in $CH_3NH_3PbI_3$ Perovskites Predicted from First-Principles. *Sci. Rep.* **2016**, *6*, 19968.

(6) Wehrenfennig, C.; Eperon, G. E.; Johnston, M. B.; Snaith, H. J.; Herz, L. M. High Charge Carrier Mobilities and Lifetimes in Organolead Trihalide Perovskites. *Adv. Mater.* **2014**, *26*, 1584−1589.

(7) Dong, Q.; Fang, Y.; Shao, Y.; Mulligan, P.; Qiu, J.; Cao, L.; Huang, J. Electron-hole diffusion lengths > 175 μm in solution-grown CH3NH3PbI3 single crystals. *Science* **2015**, *347*, 967−970.

(8) Shi, D.; Adinolfi, V.; Comin, R.; Yuan, M.; Alarousu, E.; Buin, A.; Chen, Y.; Hoogland, S.; Rothenberger, A.; Katsiev, K.; et al. Low trap-state density and long carrier diffusion in organolead trihalide perovskite single crystals. *Science* **2015**, *347*, 519−522.

(9) Huang, J.; Yuan, Y.; Shao, Y.; Yan, Y. Understanding the physical properties of hybrid perovskites for photovoltaic applications. *Nat. Rev. Mater.* **2017**, *2*, 17042.

(10) Albero, J.; Asiri, A. M.; García, H. Influence of the composition of hybrid perovskites on their performance in solar cells. *J. Mater. Chem. A* **2016**, *4*, 4353−4364.

(11) Fakharuddin, A.; Schmidt-Mende, L.; Garcia-Belmonte, G.; Jose, R.; Mora-Sero, I. Interfaces in Perovskite Solar Cells. *Adv. Energy Mater.* **2017**, *7*, 1700623.

(12) Kim, J. Y.; Lee, J.-W.; Jung, H. S.; Shin, H.; Park, N.-G. High-Efficiency Perovskite Solar Cells. *Chem. Rev.* **2020**, *120*, 7867−7918.
(13) Webb, T.; Sweeney, S. J.; Zhang, W. Device Architecture Engineering: Progress toward Next Generation Perovskite Solar Cells. *Adv. Funct. Mater.* **2021**, *31*, 2103121.
(14) Xu, H.; Yuan, F.; Zhou, D.; Liao, X.; Chen, L.; Chen, Y. Hole transport layers for organic solar cells: recent progress and prospects. *J. Mater. Chem. A* **2020**, *8*, 11478−11492.
(15) Lian, J.; Lu, B.; Niu, F.; Zeng, P.; Zhan, X. Electron-Transport Materials in Perovskite Solar Cells. *Small Methods* **2018**, *2*, 1800082.
(16) Murugan, P.; Hu, T.; Hu, X.; Chen, Y. Advancements in organic small molecule hole-transporting materials for perovskite solar cells: past and future. *J. Mater. Chem. A* **2022**, *10*, 5044−5081.
(17) Kim, G.-W.; Choi, H.; Kim, M.; Lee, J.; Son, S. Y.; Park, T. Hole Transport Materials in Conventional Structural (n−i−p) Perovskite Solar Cells: From Past to the Future. *Adv. Energy Mater.* **2020**, *10*, 1903403.
(18) Yang, X.; Wang, H.; Cai, B.; Yu, Z.; Sun, L. Progress in hole-transporting materials for perovskite solar cells. *J. Energy Chem.* **2018**, *27*, 650−672.
(19) Kung, P.-K.; Li, M.-H.; Lin, P.-Y.; Chiang, Y.-H.; Chan, C.-R.; Guo, T.-F.; Chen, P. A Review of Inorganic Hole Transport Materials for Perovskite Solar Cells. *Adv. Mater. Interfaces* **2018**, *5*, 1800882.
(20) Yan, W.; Ye, S.; Li, Y.; Sun, W.; Rao, H.; Liu, Z.; Bian, Z.; Huang, C. Hole-Transporting Materials in Inverted Planar Perovskite Solar Cells. *Adv. Energy Mater.* **2016**, *6*, 1600474.
(21) Li, Y.; Lim, E. L.; Xie, H.; Song, J.; Kong, T.; Zhang, Y.; Yang, M.; Wu, B.; Duan, C.; Bi, D. Hydrophobic Fluorinated Conjugated Polymer as a Multifunctional Interlayer for High-Performance Perovskite Solar Cells. *ACS Photonics* **2021**, *8*, 3185−3192.
(22) Ling, W.; Liu, F.; Li, Q.; Li, Z. The crucial roles of the configurations and electronic properties of organic hole-transporting molecules to the photovoltaic performance of perovskite solar cells. *J. Mater. Chem. A* **2021**, *9*, 18148−18163.
(23) Schloemer, T. H.; Christians, J. A.; Luther, J. M.; Sellinger, A. Doping strategies for small molecule organic hole-transport materials: impacts on perovskite solar cell performance and stability. *Chem. Sci.* **2019**, *10*, 1904−1935.
(24) Juarez-Perez, E. J.; Leyden, M. R.; Wang, S.; Ono, L. K.; Hawash, Z.; Qi, Y. Role of the Dopants on the Morphological and Transport Properties of Spiro-MeOTAD Hole Transport Layer. *Chem. Mater.* **2016**, *28*, 5702−5709.
(25) Wang, S.; Huang, Z.; Wang, X.; Li, Y.; Günther, M.; Valenzuela, S.; Parikh, P.; Cabreros, A.; Xiong, W.; Meng, Y. S. Unveiling the Role of tBP−LiTFSI Complexes in Perovskite Solar Cells. *J. Am. Chem. Soc.* **2018**, *140*, 16720−16730.
(26) Sun, X.; Yu, X.; Li, Z. a. Recent Advances of Dopant-Free Polymer Hole-Transporting Materials for Perovskite Solar Cells. *ACS Appl. Energy Mater.* **2020**, *3*, 10282−10302.
(27) Pham, H. D.; Yang, T. C.-J.; Jain, S. M.; Wilson, G. J.; Sonar, P. Development of Dopant-Free Organic Hole Transporting Materials for Perovskite Solar Cells. *Adv. Energy Mater.* **2020**, *10*, 1903326.
(28) Zhou, W.; Wen, Z.; Gao, P. Less is More: Dopant-Free Hole Transporting Materials for High-Efficiency Perovskite Solar Cells. *Adv. Energy Mater.* **2018**, *8*, 1702512.
(29) Rezaee, E.; Liu, X.; Hu, Q.; Dong, L.; Chen, Q.; Pan, J.-H.; Xu, Z.-X. Dopant-Free Hole Transporting Materials for Perovskite Solar Cells. *Sol. RRL* **2018**, *2*, 1800200.
(30) Wang, W.; Zhou, J.; Tang, W. Design of dopant-free small molecular hole transport materials for perovskite solar cells: a viewpoint from defect passivation. *J. Mater. Chem. A* **2022**, *10*, 1150−1178.
(31) Chen, S.; Dai, X.; Xu, S.; Jiao, H.; Zhao, L.; Huang, J. Stabilizing perovskite-substrate interfaces for high-performance perovskite modules. *Science* **2021**, *373*, 902−907.
(32) Hwang, K.; Jung, Y.-S.; Heo, Y.-J.; Scholes, F. H.; Watkins, S. E.; Subbiah, J.; Jones, D. J.; Kim, D.-Y.; Vak, D. Toward Large Scale Roll-to-Roll Production of Fully Printed Perovskite Solar Cells. *Adv. Mater.* **2015**, *27*, 1241−1247.
(33) Yan, C.; Huang, J.; Li, D.; Li, G. Recent progress of metal-halide perovskite-based tandem solar cells. *Mater. Chem. Front.* **2021**, *5*, 4538−4564.
(34) Han, W.; Ren, G.; Liu, J.; Li, Z.; Bao, H.; Liu, C.; Guo, W. Recent Progress of Inverted Perovskite Solar Cells with a Modified PEDOT:PSS Hole Transport Layer. *ACS Appl. Mater. Interfaces* **2020**, *12*, 49297−49322.
(35) Wang, Y.; Duan, L.; Zhang, M.; Hameiri, Z.; Liu, X.; Bai, Y.; Hao, X. PTAA as Efficient Hole Transport Materials in Perovskite Solar Cells: A Review. *Sol. RRL* **2022**, *6*, 2200234.
(36) Wang, M.; Wang, H.; Li, W.; Hu, X.; Sun, K.; Zang, Z. Defect passivation using ultrathin PTAA layers for efficient and stable perovskite solar cells with a high fill factor and eliminated hysteresis. *J. Mater. Chem. A* **2019**, *7*, 26421−26428.
(37) Wang, Z.; Zeng, L.; Zhang, C.; Lu, Y.; Qiu, S.; Wang, C.; Liu, C.; Pan, L.; Wu, S.; Hu, J.; et al. Rational Interface Design and Morphology Control for Blade-Coating Efficient Flexible Perovskite Solar Cells with a Record Fill Factor of 81%. *Adv. Funct. Mater.* **2020**, *30*, 2001240.
(38) Xiong, Q.; Tian, H.; Zhang, J.; Han, L.; Lu, C.; Shen, B.; Zhang, Y.; Zheng, Y.; Lu, C.; Zeng, Z.; et al. CuSCN modified PEDOT:PSS to improve the efficiency of low temperature processed perovskite solar cells. *Org. Electron.* **2018**, *61*, 151−156.
(39) Javaid, H.; Duzhko, V. V.; Venkataraman, D. Hole Transport Bilayer for Highly Efficient and Stable Inverted Perovskite Solar Cells. *ACS Appl. Energy Mater.* **2021**, *4*, 72−80.
(40) Macdonald, T. J.; Clancy, A. J.; Xu, W.; Jiang, Z.; Lin, C.-T.; Mohan, L.; Du, T.; Tune, D. D.; Lanzetta, L.; Min, G.; et al. Phosphorene Nanoribbon-Augmented Optoelectronics for Enhanced Hole Extraction. *J. Am. Chem. Soc.* **2021**, *143*, 21549−21559.
(41) Peña-Camargo, F.; Caprioglio, P.; Zu, F.; Gutierrez-Partida, E.; Wolff, C. M.; Brinkmann, K.; Albrecht, S.; Riedl, T.; Koch, N.; Neher, D.; et al. Halide Segregation versus Interfacial Recombination in Bromide-Rich Wide-Gap Perovskite Solar Cells. *ACS Energy Lett.* **2020**, *5*, 2728−2736.
(42) Mann, D. S.; Seo, Y.-H.; Kwon, S.-N.; Na, S.-I. Efficient and stable planar perovskite solar cells with a PEDOT:PSS/SrGO hole interfacial layer. *J. Alloys Compd.* **2020**, *812*, 152091.
(43) Jung, E. D.; Harit, A. K.; Kim, D. H.; Jang, C. H.; Park, J. H.; Cho, S.; Song, M. H.; Woo, H. Y. Multiply Charged Conjugated Polyelectrolytes as a Multifunctional Interlayer for Efficient and Scalable Perovskite Solar Cells. *Adv. Mater.* **2020**, *32*, 2002333.
(44) Lei, T.; Dong, H.; Xi, J.; Niu, Y.; Xu, J.; Yuan, F.; Jiao, B.; Zhang, W.; Hou, X.; Wu, Z. Highly-efficient and low-temperature perovskite solar cells by employing a Bi-hole transport layer consisting of vanadium oxide and copper phthalocyanine. *Chem. Commun.* **2018**, *54*, 6177−6180.
(45) Hemasiri, N. H.; Caliò, L.; Pegu, M.; Kazim, S.; Ahmad, S. Molecular Interface Engineering via Triazatruxene-Based Moieties/NiOx as Hole-Selective Bilayers in Perovskite Solar Cells for Reliability. *Sol. RRL* **2022**, *6*, 2100793.
(46) Gómez, P.; Georgakopoulos, S.; Más-Montoya, M.; Cerdá, J.; Pérez, J.; Ortí, E.; Aragó, J.; Curiel, D. Improving the Robustness of Organic Semiconductors through Hydrogen Bonding. *ACS Appl. Mater. Interfaces* **2021**, *13*, 8620−8630.
(47) Gómez, P.; Cerdá, J.; Más-Montoya, M.; Georgakopoulos, S.; da Silva, I.; García, A.; Ortí, E.; Aragó, J.; Curiel, D. Effect of molecular geometry and extended conjugation on the performance of hydrogen-bonded semiconductors in organic thin-film field-effect transistors. *J. Mater. Chem. C* **2021**, *9*, 10819−10829.
(48) Gómez, P.; Wang, J.; Más-Montoya, M.; Bautista, D.; Weijtens, C. H. L.; Curiel, D.; Janssen, R. A. J. Pyrene-Based Small-Molecular Hole Transport Layers for Efficient and Stable Narrow-Bandgap Perovskite Solar Cells. *Sol. RRL* **2021**, *5*, 2100454.
(49) Más-Montoya, M.; Gómez, P.; Curiel, D.; da Silva, I.; Wang, J.; Janssen, R. A. J. A Self-Assembled Small-Molecule-Based Hole-Transporting Material for Inverted Perovskite Solar Cells. *Chem. Eur. J.* **2020**, *26*, 10276−10282.

(50) Rodríguez, L. M.; Gómez, P.; Más-Montoya, M.; Abad, J.; Tárraga, A.; Cerdá, J. I.; Méndez, J.; Curiel, D. Synthesis and Two-Dimensional Chiral Surface Self-Assembly of a π-Conjugated System with Three-Fold Symmetry: Benzotri(7-Azaindole). *Angew. Chem., Int. Ed.* **2021**, *60*, 1782−1788.
(51) Cui, B.-B.; Yang, N.; Shi, C.; Yang, S.; Shao, J.-Y.; Han, Y.; Zhang, L.; Zhang, Q.; Zhong, Y.-W.; Chen, Q. Naphtho[1,2-*b*:4,3-*b*′]dithiophene-based hole transporting materials for high-performance perovskite solar cells: molecular engineering and opto-electronic properties. *J. Mater. Chem. A* **2018**, *6*, 10057−10063.
(52) Guo, H.; Zhang, H.; Shen, C.; Zhang, D.; Liu, S.; Wu, Y.; Zhu, W.-H. A Coplanar π-Extended Quinoxaline Based Hole-Transporting Material Enabling over 21% Efficiency for Dopant-Free Perovskite Solar Cells. *Angew. Chem., Int. Ed.* **2021**, *60*, 2674−2679.
(53) Chang, Z.; Guo, J.; Fu, Q.; Wang, T.; Wang, R.; Liu, Y. Central-Core Engineering of Dopant-Free Hole Transport Materials for Efficient n-i-p Structured Perovskite Solar Cells. *Sol. RRL* **2021**, *5*, 2100184.
(54) D'Alterio, M. C.; Casals-Cruañas, È.; Tzouras, N. V.; Talarico, G.; Nolan, S. P.; Poater, A. Mechanistic Aspects of the Palladium-Catalyzed Suzuki-Miyaura Cross-Coupling Reaction. *Chem. Eur. J.* **2021**, *27*, 13481−13493.
(55) Hostyn, S.; Van Baelen, G.; Lemière, G. L. F.; Maes, B. U. W. Synthesis of α-Carbolines Starting from 2,3-Dichloropyridines and Substituted Anilines. *Adv. Synth. Catal.* **2008**, *350*, 2653−2660.
(56) Schneider, C.; Gueyrard, D.; Popowycz, F.; Joseph, B.; Goekjian, P. G. Synthesis of 6-Substituted Pyrido[2,3-*b*]indoles by Electrophilic Substitution. *Synlett* **2007**, *2007*, 2237−2241.
(57) Tsuji, H.; Ota, Y.; Furukawa, S.; Mitsui, C.; Sato, Y.; Nakamura, E. Tripyridyltruxenes: Thermally Stable Cathode Buffer Materials for Organic Thin-Film Solar Cells. *Asian J. Org. Chem.* **2012**, *1*, 34−37.
(58) Kotha, S.; Ali, R.; Panguluri, N. R.; Datta, A.; Kannaujiya, K. K. Synthesis and photophysical properties of star-shaped blue green emitting π-conjugated spirotruxenes. *Tetrahedron Lett.* **2018**, *59*, 4080−4085.
(59) Ruiz-Castillo, P.; Buchwald, S. L. Applications of Palladium-Catalyzed C−N Cross-Coupling Reactions. *Chem. Rev.* **2016**, *116*, 12564−12649.
(60) Gómez, P.; Georgakopoulos, S.; Cerón, J. P.; da Silva, I.; Más-Montoya, M.; Pérez, J.; Tárraga, A.; Curiel, D. Hydrogen-bonded azaphenacene: a strategy for the organization of π-conjugated materials. *J. Mater. Chem. C* **2018**, *6*, 3968−3975.
(61) Murgatroyd, P. N. Theory of space-charge-limited current enhanced by Frenkel effect. *J. Phys. D: Appl. Phys.* **1970**, *3*, 151.
(62) Khadka, D. B.; Shirai, Y.; Yanagida, M.; Ryan, J. W.; Miyano, K. Exploring the effects of interfacial carrier transport layers on device performance and optoelectronic properties of planar perovskite solar cells. *J. Mater. Chem. C* **2017**, *5*, 8819−8827.
(63) Rong, Y.; Hu, Y.; Ravishankar, S.; Liu, H.; Hou, X.; Sheng, Y.; Mei, A.; Wang, Q.; Li, D.; Xu, M.; et al. Tunable hysteresis effect for perovskite solar cells. *Energy Environ. Sci.* **2017**, *10*, 2383−2391.
(64) Sanchez, R. S.; Gonzalez-Pedro, V.; Lee, J.-W.; Park, N.-G.; Kang, Y. S.; Mora-Sero, I.; Bisquert, J. Slow Dynamic Processes in Lead Halide Perovskite Solar Cells. Characteristic Times and Hysteresis. *J. Phys. Chem. Lett.* **2014**, *5*, 2357−2363.
(65) Almora, O.; Baran, D.; Bazan, G. C.; Berger, C.; Cabrera, C. I.; Catchpole, K. R.; Erten-Ela, S.; Guo, F.; Hauch, J.; Ho-Baillie, A. W. Y.; et al. Device Performance of Emerging Photovoltaic Materials (Version 2). *Adv. Energy Mater.* **2021**, *11*, 2102526.
(66) Tress, W.; Yavari, M.; Domanski, K.; Yadav, P.; Niesen, B.; Correa Baena, J. P.; Hagfeldt, A.; Graetzel, M. Interpretation and evolution of open-circuit voltage, recombination, ideality factor and subgap defect states during reversible light-soaking and irreversible degradation of perovskite solar cells. *Energy Environ. Sci.* **2018**, *11*, 151−165.
(67) Stolterfoht, M.; Le Corre, V. M.; Feuerstein, M.; Caprioglio, P.; Koster, L. J. A.; Neher, D. Voltage-Dependent Photoluminescence and How It Correlates with the Fill Factor and Open-Circuit Voltage in Perovskite Solar Cells. *ACS Energy Lett.* **2019**, *4*, 2887−2892.
(68) Du, T.; Xu, W.; Daboczi, M.; Kim, J.; Xu, S.; Lin, C.-T.; Kang, H.; Lee, K.; Heeney, M. J.; Kim, J.-S.; et al. p-Doping of organic hole transport layers in p−i−n perovskite solar cells: correlating open-circuit voltage and photoluminescence quenching. *J. Mater. Chem. A* **2019**, *7*, 18971−18979.
(69) Siebentritt, S.; Weiss, T. P.; Sood, M.; Wolter, M. H.; Lomuscio, A.; Ramirez, O. How photoluminescence can predict the efficiency of solar cells. *J. Phys-Mater.* **2021**, *4*, No. 042010.
(70) Kirchartz, T.; Márquez, J. A.; Stolterfoht, M.; Unold, T. Photoluminescence-Based Characterization of Halide Perovskites for Photovoltaics. *Adv. Energy Mater.* **2020**, *10*, 1904134.
(71) Neophytou, M.; Griffiths, J.; Fraser, J.; Kirkus, M.; Chen, H.; Nielsen, C. B.; McCulloch, I. High mobility, hole transport materials for highly efficient PEDOT:PSS replacement in inverted perovskite solar cells. *J. Mater. Chem. C* **2017**, *5*, 4940−4945.
(72) Daboczi, M.; Hamilton, I.; Xu, S.; Luke, J.; Limbu, S.; Lee, J.; McLachlan, M. A.; Lee, K.; Durrant, J. R.; Baikie, I. D.; et al. Origin of Open-Circuit Voltage Losses in Perovskite Solar Cells Investigated by Surface Photovoltage Measurement. *ACS Appl. Mater. Interfaces* **2019**, *11*, 46808−46817.
(73) Yoo, S.-M.; Yoon, S. J.; Anta, J. A.; Lee, H. J.; Boix, P. P.; Mora-Seró, I. An Equivalent Circuit for Perovskite Solar Cell Bridging Sensitized to Thin Film Architectures. *Joule* **2019**, *3*, 2535−2549.

https://doi.org/10.1021/acsami.2c23010
ACS Appl. Mater. Interfaces 2023, 15, 22310−22319